ACS APPLIED MATERIALS & INTERFACES
Research Article
www.acsami.org

Growth of Crystalline Hydroxyapatite Thin Films at Room Temperature by Tuning the Energy of the RF-Magnetron Sputtering Plasma

Elvis O. López, Alexandre Mello, Henrique Sendão, Lilian T. Costa, André L. Rossi, Rogelio O. Ospina, Fabrício F. Borghi, José G. Silva Filho, and Alexandre M. Rossi*

Department of Applied Physics, Brazilian Center for Physics Research, Urca, Rio de Janeiro 22290-180, Brazil

ABSTRACT: Right angle radio frequency magnetron sputtering technique (RAMS) was redesigned to favor the production of high-quality hydroxyapatite (HA) thin coatings for biomedical applications. Stoichiometric HA films with controlled crystallinity, thickness varying from 254 to 540 nm, crystallite mean size of 73 nm, and RMS roughness of 1.7 ± 0.9 nm, were obtained at room temperature by tuning the thermodynamic properties of the plasma sheath energy. The plasma energies were adjusted by using a suitable high magnetic field confinement of 143 mT (1430 G) and a substrate floating potential of 2 V at the substrate-to-magnetron distance of Z = 10 mm and by varying the sputtering geometry, substrate-to-magnetron distance from Z = 5 mm to Z = 18 mm, forwarded RF power and reactive gas pressure. Measurements that were taken with a Langmuir probe showed that the adjusted RAMS geometry generated a plasma with an adequate effective temperature of $T_{eff} \approx 11.8$ eV and electron density of 2.0×10^{15} m^{-3} to nucleate nanoclusters and to further crystallize the nanodomains of stoichiometric HA. The deposition mechanism in the RAMS geometry was described by the formation of *building units* of amorphous calcium phosphate clusters (ACP), the conversion into HA nanodomains and the crystallization of the grain domains with a preferential orientation along the HA [002] direction.

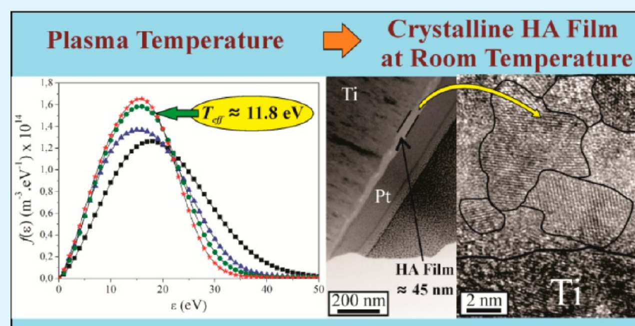

KEYWORDS: *hydroxyapatite, thin films, rf magnetron sputtering, plasma thermodynamics, biomaterial, bioengineering*

1. INTRODUCTION

Hydroxyapatite (HA), $Ca_{10}(PO_4)_6(OH)_2$,[1,2] is a biomaterial that is commonly used in biomedical applications that involve bone substitution and bone regeneration because of its excellent biocompatibility, high bioactivity, and good osseoconductivity.[3,4] Because biocompatible metals are poorly bioactive, coating techniques with calcium phosphate have been developed to improve the osseointegration of metallic implants.[5−10] The plasma spray technique is commercially used to produce calcium phosphate coatings on titanium implants because of its low cost and high deposition rates. However, plasma spray deposition operates at a high temperature, which occasionally induces the formation of secondary mineral phases, such as tricalcium phosphate (TCP) and calcium oxide (CaO).[11−13] Additionally, the coating crystallinity and roughness are not easily controlled during the deposition process. In the past few years, significant efforts have been made to improve plasma spray coating adhesion.[14] Additionally, several alternative coating techniques have been proposed that use different deposition principles. The most common techniques are biomimetics,[15] sol−gel routes,[16−18] electrochemical deposition,[10,19−21] and other possible chemical deposition processes,[22,23] as well as the physical deposition by pulsed laser (PLD),[24,25] ion beam deposition,[26,27] and radio frequency magnetron sputtering (RF-MS).[28,29] The challenges for these techniques are the control of the coating stoichiometry, the coating adhesion to the implant surface and the formation of amorphous phases during the deposition process, which require a subsequent heat treatment at a high temperature. Latest advances on calcium phosphates coatings produced by several deposition techniques were recently reviewed by Surmenev and Dorozhkin.[30,31]

Several studies have shown that the radio frequency magnetron sputtering technique (RF-MS) has potential for biomedical applications because it might produce nanostructured coatings with low surface roughness and good adhesion to the substrate.[32,33] On the other hand, the inadequate sputtering energy that is caused by the RF power that is applied to the magnetrons and the gas pressure, as well as the geometry of the sputtering system, inhibit the growth of films with the correct stoichiometry.[32−36] These limitations could be overcome by fixing the targets at the extremities of two opposite magnetrons with parallel faces and by positioning the substrate at a right angle with respect to the magnetrons.[37]

Received: May 27, 2013
Accepted: September 9, 2013
Published: September 9, 2013

 © 2013 American Chemical Society

This alternative geometry could generate deposition rates 50 times higher (1000 Å/min) than those of the conventional magnetron sputtering geometry. The right angle geometry was adapted by Mello and our group[38,39] for the production of hydroxyapatite thin films. These authors magnetically confined the plasma and kept it away from the substrate surface (floating substrate holder) to limit backsputtering effects.[40] Under this condition, more stoichiometric hydroxyapatite thin films could be produced, thus revealing new possibilities for producing biocompatible thin coatings for biomedical applications. However, the conditions that are needed to produce controlled and reproducible thin coatings using the right angle magnetron sputtering (RAMS) geometry are not yet well-known due to (i) the lack of studies on the thermodynamic properties of the plasma that is produced by RAMS and (ii) the kinetics mechanisms of a HA thin film growing over different substrates. This work aims to obtain new information and propose solutions concerning these two aspects. First, we analyzed some thermodynamic parameters of the RAMS plasma, such as the effective temperature (T_{eff}), electron density (n_e), and potential (V_p) of the plasma edge, using Langmuir probe measurements.[41] Second, we analyzed the magnetic field flux ($\boldsymbol{B}$) in the sputtering chamber using magnetic measurements that were obtained with a Hall probe[42] and were processed by a finite elements method. Afterward, we showed how the thin film structure depends on the plasma parameters that can be adjusted by using a suitable high plasma magnetic field confinement, adequate RF power and reactive gas pressure, substrate floating potential, and by varying the sputtering geometry, substrate-to-magnetron distance. Based on these data, we propose a mechanism for thin film growth on substrate surfaces, mainly metallic surfaces for biomedical applications.

2. EXPERIMENTAL SECTION

2.1. Hydroxyapatite Synthesis and Target Preparation. The synthesis of stoichiometric hydroxyapatite, HA, was performed by wet precipitation (T = 90 °C, pH = 11.0 and 2 h of aging time) from aqueous solutions of calcium nitrate ($Ca(NO_3)_2 \cdot 4H_2O$) and diammonium phosphate $(NH_4)_2HPO_4$. After aging, the precipitate was separated by filtration, repeatedly washed with deionized boiling water and dried in an oven at 100 °C for 24 h. After drying, the powder was manually ground, and micrometric particles with 77 μm < d < 210 μm were separated by sieving. Cylindrical tablets 35 mm in diameter and 4 mm high were prepared by uniaxially pressing the HA powder under 51 MPa. HA targets were produced by sintering the tablets at 1150 °C for 2 h.

The XRD pattern of the HA target that was annealed at 1150 °C, as shown in Figure 1a, exhibited peaks due to the high crystalline of HA (ICDD N° 84−1998).[43] Typical peaks that are due to HA decomposition phases, such as tricalcium phosphate (β-TCP) and calcium oxide (CaO), were not detected. The cell parameters (a = b and c)[44] were a = 0.94103 nm and c = 0.68746 nm, close to those of stoichiometric HA (a = 0.94166 nm and c = 0.68745 nm, ICDD N° 84−1998).[43] The FTIR spectra of the targets were typical of HA with the vibration modes of $(PO_4)^{3-}$ at 1088 cm^{-1}, 1016 cm^{-1} and 964 cm^{-1} and the $(OH)^-$ band at 3570 cm^{-1}

A second series of targets was prepared from calcium deficient hydroxyapatite, DHA, following the same procedure as that for stoichiometric HA. Because DHA was unstable against thermal treatment at high temperatures, the calcinations at 1150 °C for 2 h induced the decomposition of the structure into three calcium phosphate phases: β-tricalcium phosphate (β-TCP), CaO, and HA, as shown in the XRD patterns (Figure 1b).

2.2. Film Preparation by RAMS. The RAMS technique with the right-angle geometry has been described in detail elsewhere.[36,37] The equipment that was used in this work had two radio frequency magnetrons (13.56 MHz) with surface areas of 507 mm^2. These magnetrons were positioned face-to-face to one another and perpendicular to the substrate (Figure 2a). The magnetic flux, $\boldsymbol{B}$, that was measured midway between the magnetrons was 143 mT and decreased to $\boldsymbol{B}$ = 0 T at Z = 14 mm. In this configuration, a floating potential substrate was positioned near in the region without the magnetic field to active the deposition of CaP particles on the substrate. A mixture of argon (Ar) and reactive oxygen (O_2) was used to produce the plasma in the sputtering chamber. Silicon (001) substrates (121 mm^2) were used and ultrasonically cleaned with acetone and deionized water for 15 min. Afterward, these substrates were chemically treated with hydrofluoric acid (5% M) for 1 min to remove the native oxide and then dried with ionized hydrogen gas at high pressure. The RMS roughness of Si (001) substrates was 0.25 ± 0.05 nm. The substrate was rotated during film deposition to homogenize the film thickness. The deposition rate for the fabrication of thin films was calibrated using a thickness measurement, which was calculated from the X-ray profile at a low angle (1° < 2θ < 5°).[45] Different series of coatings were produced, as shown in Table 1. The first, second, fourth, and fifth film series were prepared with the stoichiometric HA targets, as shown in Figure 1a, while the third series was prepared with the calcium deficient hydroxyapatite targets, as shown in Figure 1b. The HA thin film that was deposited on a Ti coating (Figure 6) was fabricated using the fourth series conditions that are listed in Table 1.

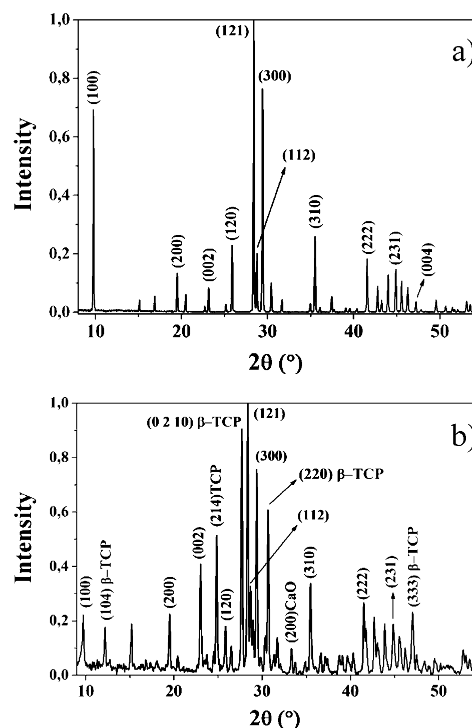

Figure 1. XRD (λ = 0.13775 nm) of the targets produced from (a) stoichiometric hydroxyapatite and (b) calcium deficient hydroxyapatite (DHA) showing the peaks of (β-TCP), CaO and HA phase.

2.3. Plasma Characterization. The plasma was characterized with a cylindrical Langmuir probe at different substrate holder positions, Z (Figure 2a). The voltage (V_B) and current (I) values that were obtained from the Langmuir probe were used in eq 1 to determine the electron energy distribution function (EEDF), $f(\varepsilon)$, at the edge of the plasma.[41] From $f(\varepsilon)$, the electron density (n_e), average energy of the electrons ($\langle E \rangle$), and effective plasma temperature (T_{eff}) could be determined for each substrate position (Z) using eqs 1−4, where m is the electron mass, e is the electron charge, A is the area of the cylindrical probe tip (with radius R = 0.4 mm and length L = 3.5 mm), $V = V_p - V_B$, and V_p is the plasma potential that can be calculated from the maximum value (dI/dV_B).[41]

Table 1. Summary of the Film Fabrications with Different Deposition Variables

series	pressure Ar (mTorr)	pressure O_2 (mTorr)	RF power (W)	dep. time (min)	height (Z) (mm)	dep. rate (nm/min)	substrate
first	5	1	120	0.5, 1, 2, 3	10	5.2	Si(001)
second	5	1	120	5, 30, 60, 180	10	5.2	Si(001)
third	5	1	120	15, 30, 45, 60, 90, 120, 150, 180	10	5.2	Si(001)
fourth	5	1	120	5, 15, 25, 30, 45, 60, 75	13	3.0	Si(001)
fifth	5	1	90, 100, 110, 120	180	10	5.2	Si(001)

$$f(\varepsilon) = \frac{2}{e^2 A}\left(\frac{2m\varepsilon}{e}\right)^{1/2}\frac{d^2 I}{dV^2} \quad (1)$$

$$n_e = \int_0^\infty f(\varepsilon)d\varepsilon \quad (2)$$

$$\langle\varepsilon\rangle = \frac{1}{n_e}\int_0^\infty \varepsilon f(\varepsilon)d\varepsilon \quad (3)$$

$$T_{eff} = \frac{2}{3}\langle\varepsilon\rangle \quad (4)$$

2.4. Target and Thin Coating Characterization. The HA targets and coatings were analyzed by X-ray diffraction (XRD) using synchrotron radiation with an energy of 9 keV (λ = 0.13775 nm) at the Brazilian Synchrotron Light Laboratory (LNLS, Campinas-Brazil). The XRD patterns were recorded in the grazing-incidence X-ray diffraction mode (GIXRD) at Φ = 0.5° and with 2θ varying from 8° to 55°, a step size of 0.025°, and a scan time of approximately 35 min (120 000 counting light/step). The lattice parameters $a = b$ and c were determined in accordance with the literature by Cullity.[44] The crystallite mean size was determined by the Williamson-Hall method.[46,47]

The vibrational spectra of the samples were obtained from a Shimadzu AIM 8800 FTIR - Fourier transformed infrared spectrometer that was connected to a microscope operating in the attenuated total reflectance mode (ATR). The spectra were obtained from a 432 μm × 332 μm area with the wavenumber varying from 750 to 4000 cm^{-1} and with 150−300 scans per sample.

The elemental composition of the films was analyzed by X-ray photoelectron spectroscopy using a SPECS PHOIBOS 100/150 spectrometer with a hemispheric analyzer operating at an X-ray energy of 1486.6 eV from Al Kα radiation. In this work, we used a source of polychromatic X-rays and a monochromator mirror with energy step of 0.02 eV (for high resolution). The polychromatic X-ray source used (Al−Kα) of the Ag $3d_{5/2}$ having fwhm = 0.8 eV while the fwhm of the monochromator mirror was 0.5 eV. The peak fitting of the high resolution measurement (by integrating the Ca, P and O peaks) was determined with the CASA-XPS software. The calibration energy that was used was C 1s (284.6 eV). The difference in the $2p_{3/2}$ and $2p_{1/2}$ levels for the phosphorus peak was $\Delta(2p_{3/2} - 2p_{1/2})$ = 0.84 eV, and for the calcium peak, the difference was $\Delta(2p_{3/2} - 2p_{1/2})$ = 3.5 eV.[48]

The coatings topographies were analyzed by scanning probe microscopy (SPM) using an INTEGRA NT-MDT and by atomic force microscopy (AFM) using JPK Nanowizard instruments (JPK instruments AG, Germany). The measurements were performed in tapping and contact mode using a tip scanner with a radius of curvature of 10 nm. The calibration parameters, which were measured as the resonance frequency of the tip, phase, amplitude, and gain, were varied for each sample.

The sample (fourth series, Table 1) that was used for the high resolution transmission electron microscopy (HRTEM) analysis was prepared with the focused ion beam (FIB) technique using dual beam FEI Nova 600 Nanolab equipment. The process consisted of (i) depositing Pt on the surface of the HA thin film, (ii) making a small cross section in the sample by sputtering layer-by-layer with a Ga ion source, and (iii) leaving a small portion of the sample at most 100 nm thick (the thickness of the sample cut).

The sample that was prepared by FIB was analyzed using high resolution transmission electron microscopy (HRTEM) and scanning transmission electron microscopy (STEM) with a JEOL 2100F operated at 200 kV. High resolution images were analyzed using the Digital Micrograph software (Gatan), from which fast Fourier transforms (FFT) were obtained. TEM observations were made using the minimum dose to prevent sample damage.

3. RESULTS AND DISCUSSION

3.1. The RAMS Geometry and Plasma Characterization. In the RAMS geometry, shown in Figure 2a, the sample holder (substrate) is maintained at a right angle to the axis of the two magnetrons. The magnetrons are composed of two insulated Cu coaxial tubes. The 1-in. diameter cathodes, which contain NdFeB magnets (N40), are connected to a 300 W, 13.56 MHz RF power supply that is coupled to a matching network. The cathode produces a magnetic field flux (***B***) that confines the electrons, generating an Ar + O_2 plasma glow in a small region at the center of the cathodes, as shown in Figure 2b. A floating potential substrate is positioned near in the region where ***B*** = 0 T (Tesla) (Z = 14 mm), thus minimizing the production of Ar^+ ions and avoiding a possible sputtering effect on the films. Under this condition, the substrate could be positioned at the edge of the plasma sheath to maximize the energy that is delivered to the substrate surface.

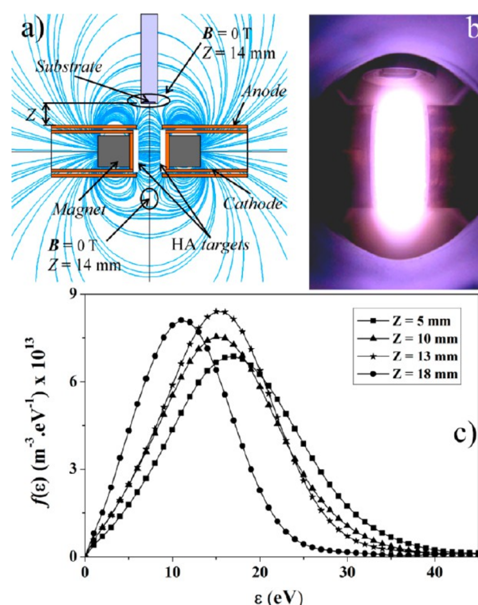

Figure 2. (a) Scheme of the RAMS system deposition chamber showing the magnetic field flux lines and the substrate position in the ***B*** ≈ 0 T regions. (b) Picture of the interior of the sputtering chamber showing the confined plasma glow at 120 W of RF power and at Ar and O_2 gas pressures of 5 mTorr and 1 mTorr, respectively. (c) Electron energy distribution function, $f(\varepsilon)$, as determined from Druyvesteyn fitting using the experimental values of V_B−I (potential source vs current) at different positions (Z) of the plasma sheath.

Table 2. Values of V_p, n_e, $\langle E \rangle$, and T_{eff} at Different Z Positions Obtained from eqs 1−4

plasma parameters	center of magnetrons	Z_1 = 5 mm	Z_2 = 10 mm	Z_3 = 13 mm	Z_4 = 18 mm
V_p (V)	−30	46	48	49	46
$n_e \times 10^{15}$ (m^{-3})	0.5	2.16	2.10	2.0	1.46
$\langle E \rangle$ (eV)	24.7	21.5	17.5	17.7	15.5
T_{eff} (eV)	16.4	14.3	11.7	11.8	10.3

Scheme 1[a]

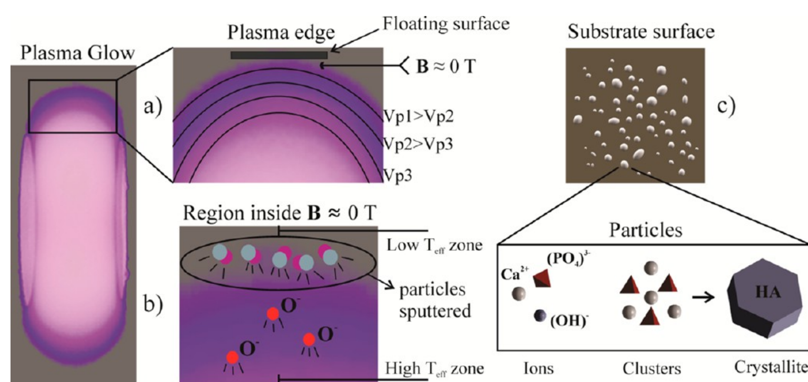

[a](a) Plasma glow (120 W of power and a gas pressure of 5 mTorr (Ar) and 1 mTorr (O_2)) and plasma edge showing the different plasma potentials (V_p) at the different plasma sheath heights. (b) Region of the plasma edge visualizing the kinetic process of the ions and particles sputtered within the plasma. (c) Illustration of the ions, clusters, and particles deposited on the substrate surface at early times and the formation of the HA phase.

From the Langmuir probe measurements, it was possible to map the applied voltage (V_B) × current (I) function around the plasma sheath region and to calculate the electron energy distribution function, $f(\varepsilon)$ (eq 1, section 2),[41,49] for different values of Z, as shown in Figure 2c. The slight movement of the function, $f(\varepsilon)$, to the left indicates an increase in cold electrons (low energy) as the height Z increases, which slightly affects the properties of the plasma. The plasma potential (V_p), electron density (n_e), average electron energy ($\langle E \rangle$), and effective plasma temperature (T_{eff}) at different Z positions were obtained from eqs 2−4 (see section 2), as shown in Table 2.

3.2. Mechanism of Film Growth. From the plasma parameters (T_{eff}, n_e, and V_p) that were calculated at different Z (Table 2), it was found that the plasma potential increased with Z. This phenomenon occurs due to the different charged particles that were sputtered from the target. These particles could be ions, clusters of atoms, radicals, nanoclusters, or agglomerates[50,51] that are transported to regions far away from the plasma sheath (low temperature regions) (Scheme 1a). The positive potential at the edge of the plasma sheath induces a flow of negatives ions (O^- and radicals PO_4^{3-}), which can be very important for the recombination of charges close to the substrate surface and to the stabilization of the film stoichiometry (Scheme 1b). Another feature of the RAMS system is the use of a substrate holder floating configuration, which is maintained at a positive potential of approximately 2 V and brakes the positive particles that reach the substrate surface while avoiding a sputtering effect on the film. On the nanometer scale, the temperature of the substrate surface increases due to the impact of the particles (electrons, ions and neutral particles) that arrive at the substrate with a Bohm velocity and a kinetic energy on the order of $T_{eff}/2$.[41] Depending on their kinetic energy, particles may react with the surface and diffuse into the substrate lattice.[5,12,52] In a state of thermal equilibrium between the plasma sheath and the substrate surface, the temperature on the surface could be sufficiently high to favor the growth of a crystalline thin film and to modify the film surface morphology.[53] However, the film growing process needs some deposition time to reach thermal equilibrium[41] which depends on the ion energy that is delivered to the substrate surface and deposition time: the greater the energy delivered to the substrate, the lower the deposition time needed to achieve a steady state.

In the RAMS geometry, high values of T_{eff} and $\langle E \rangle$ were obtained for different regions of the plasma. In the center of the magnetrons, the effective plasma temperature achieved a value of T_{eff} = 16.4 eV while the average electron energy was $\langle E \rangle$ = 24.7 eV. These energies were sufficiently high to promote the dissociation of P−O ($E_{diss} \approx 6$ eV) and Ca−O ($E_{diss} \approx 5$ eV) bonds leading the formation of ionic species.[54,55] Within the plasma sheath region around the position where the external magnetic field was close to zero T_{eff} and $\langle E \rangle$ decreased to 11.7 and 17.5 eV, respectively, which are above the energy that is required to produce a Posner's cluster of $[Ca_3(PO_4)_2]_3$ and to crystallize hydroxyapatite (Scheme 1c) as shown in Table 2 and represented in Scheme 1b. According to the work of Treboux and group,[56] the activation energy that is needed to form Posner's clusters from monomers, $Ca_3(PO_4)_2$, should be 4.3 eV, while the energy that is needed to crystallize hydroxyapatite is approximately 2.6 eV.[57] This result showed that the initial condition to crystallize hydroxyapatite is satisfied in the RAMS geometry if the substrate is placed at the edge of the plasma sheath region because the plasma temperature keeps the deposited particles in a high energy state, thus facilitating the mobility of the atoms at the substrate surface and leading to HA precursor clusters at short deposition times.

3.2.1. Stoichiometry. A first series of films was produced with low deposition times to determine the evolution of the stoichiometry with increasing film thickness. Deposition times of 30, 60, 120, and 180 s led to films with 2.6, 5.2, 10.4, and 15.6 nm thicknesses, respectively. XPS (Al Kα) high resolution analysis was conducted for all thin films and showed a calcium-

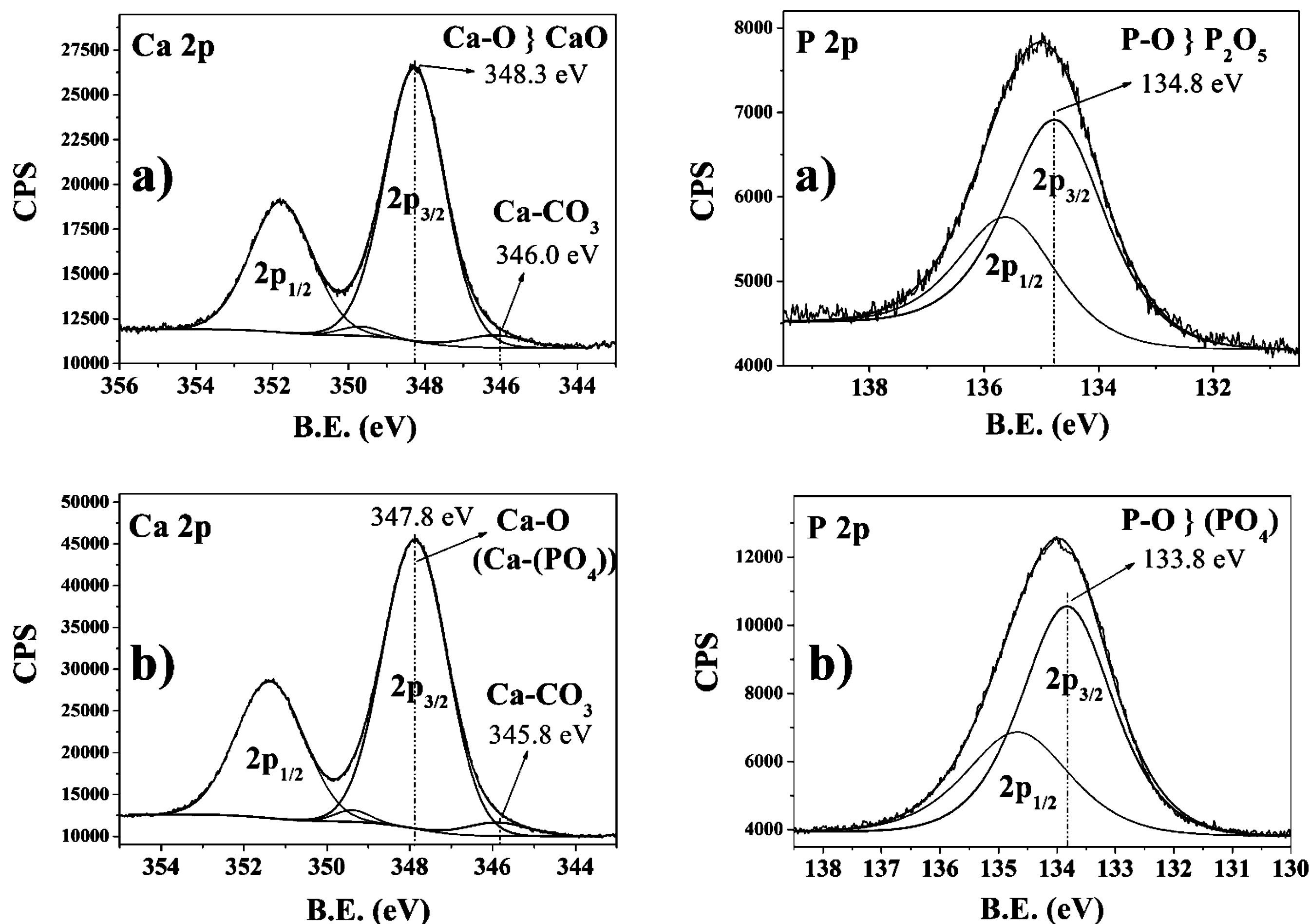

Figure 3. XPS spectra of the CaP film deposited for (a) 30 s (thickness of 2.6 nm) and (b) 180 s (thickness of 15.6 nm) showing the high resolution spectrum of Ca 2p and P 2p peak fitting. The films were made at a deposition rate of 5.2 nm/min (Z = 10 mm) with a plasma power of 120 W and gas pressures of 5 mTorr and 1 mTorr for argon and oxygen (T_{eff} = 11.7 eV).

to-phosphate ratio (Ca/P = 1.20 ± 0.09 and O/P = 4.25 ± 0.96). For the 2.6 nm thickness film (deposition time of 30 s), the Ca $2p_{3/2}$ envelope was fitted with two peaks as observed in Figure 3a: (i) first peak was fitted as the orbital Ca $2p_{3/2}$ = 348.3 eV and was attributed to the Ca−O binding energy from CaO;[58] (ii) the second weak peak fitted as the orbital Ca $2p_{3/2}$ at 346.2 eV was attributed to the Ca−CO_3 binding energy due to carbon species adsorbed form the air.[48,59] The P 2p envelope was fitted with one P $2p_{3/2}$ component at 134.8 eV, which was attributed to the P−O bindings in P_2O_5.[48,60] This result justified the assumption of excessive amount of phosphorus containing species and the low Ca/P that was found for the 30 s film. In addition, these results also reinforced the hypothesis described in section 3.2 in which the high energy delivered by RAMS plasma favored the production of free ions and small Ca and P ionic species which diffuse across the high energy plasma sheath toward the substrate surface. These ions reacted on the film surface inducing the formation of Ca and P nanoclusters such as CaO and P_2O_5 in the early stage of the film growth. It can be assumed that these complex clusters constituted the primary film with amorphous compounds produced by RAMS at the beginning of the deposition process. Furthermore, the high values of T_{eff} and $\langle E \rangle$ still present within the plasma sheath region (Z = 10 mm and Z = 13 mm) at this stage of the film growth was an important factor to inhibit the deposition of large nanoclusters at the substrate surface keeping the film roughness at low levels (roughness ≤ 4 nm).

As the deposition time increases, more energy is delivered to the substrate, which may be used to reorganize the *building units*[50] into calcium phosphate domains, as illustrated in Scheme 1c. The nucleation of HA from amorphous Posner clusters, $(Ca_3(PO_4)_2)_3$, that may coexist with CaO monomers, was observed in ab initio calculations that were conducted by Wang and by Gabin Treboux.[2,56] The change of the film composition with the deposition time and the formation of the first calcium phosphate *building units*[50] was detected in the analysis of XPS spectrum of the film deposited for 180 s. The fitting of Ca 2p and P 2p peaks, Figure 3b, showed that Ca $2p_{3/2}$ and P $2p_{3/2}$ binding energy correspond to those of Ca−O and P−O bonds in a calcium phosphate phase (347.8 and 133.8 eV respectively).[61,62] Reinforcing the conclusions above, peaks relative to Ca−O bonds in CaO (348.3 eV) and the P−O bond in P_2O_5 (134.8 eV) were no longer present in those 180 s films. The low Ca/P ratio (Ca/P = 1.2) may be attributed to the nucleation of an amorphous calcium phosphates, ACP ($Ca_9(PO_4)_{6-x}(HPO_4)_x(OH)_x$, Ca/P ratio varying from 1.15 to 2.2).[63]

The final stage of the conversion of ACP to stoichiometric hydroxyapatite was investigated by XPS with film deposited for 180 min (the second series of films prepared − Table 1). The XPS measurements of samples were obtained using argon ion

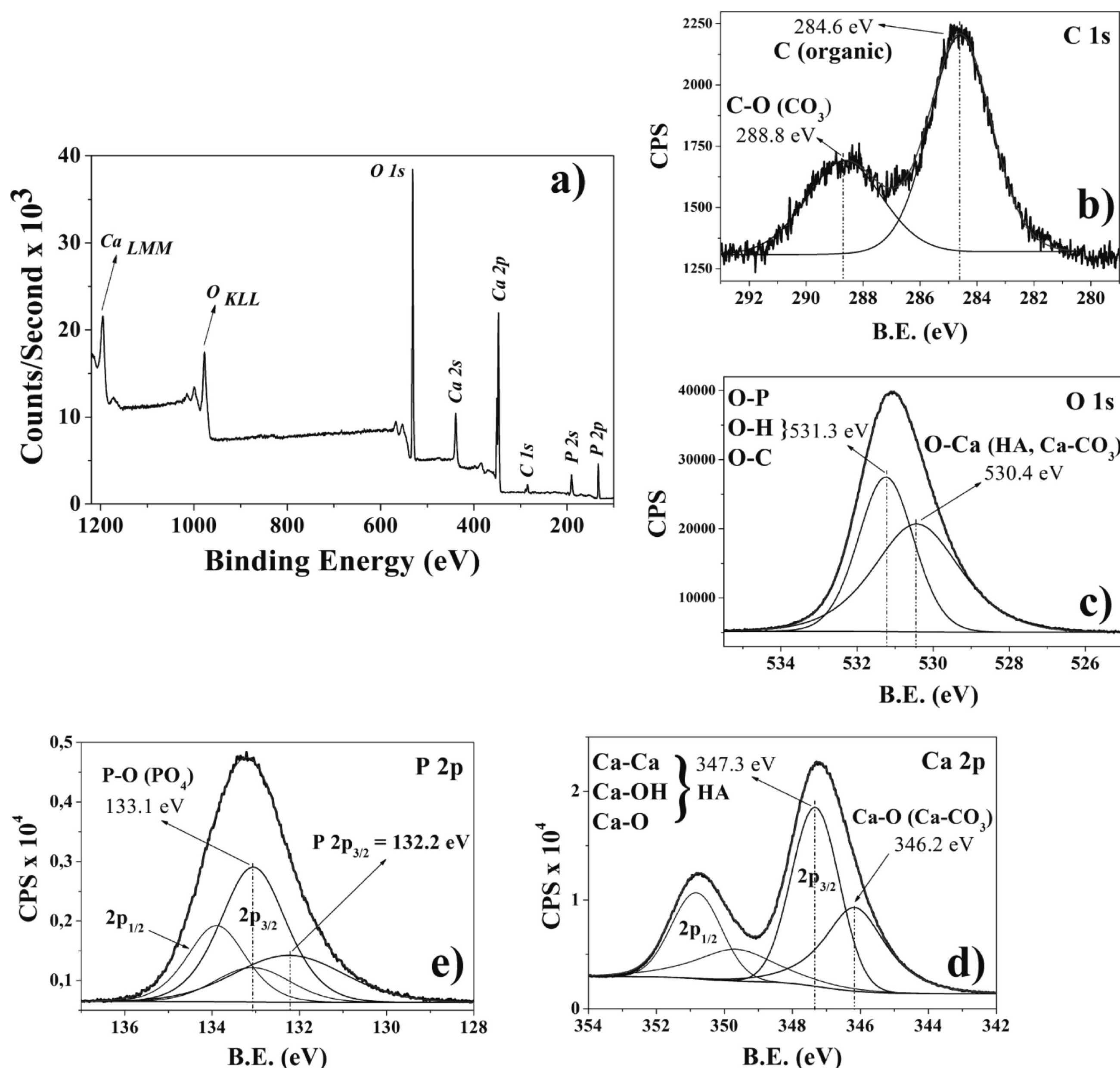

Figure 4. XPS spectra of the HA film deposited for 180 min (thickness of 930 nm) showing (a) the full spectrum with slight etching by Ar ions and the high resolution spectrum for the (b) C 1s, (c) O 1s, (d) Ca 2p, and (e) P 2p peaks. The film was made at a deposition rate of 5.2 nm/min (Z = 10 mm) with a plasma power of 120 W and gas pressures of 5 mTorr and 1 mTorr for argon and oxygen (T_{eff} = 11.7 eV).

etching to remove any impurities adhered on the film surface. The energy and time that were used in this treatment were low (1 keV and 2 min) to avoid Ar ion implantation, which may affect the film stoichiometry. The full scan of the film (deposited at 180 min) presented typical peaks at binding energy that corresponded to Ca 2p, P 2p, and O 1s, as shown in Figure 4a. The peak fitting for 180 min films over the carbon C 1s region (Figure 4b) have shown binding energy of C 1s = 284.6 eV (organic species), used to adjust the spectra[64] and the C 1s = 288.8 eV which was attributed to C−O bindings in carbonate ions (CO_3^{2-}).[48] The high resolution peak O 1s (fwhm = 2.2 eV), Figure 4c, was fitted with two energies: (i) O 1s = 531.3 eV for the oxygen binding energy from the phosphates groups $(PO_4)^{3-}$, OH^- groups, and CO_3^{2-} groups, which are inseparable by peak fitting routine, and[59] (ii) O 1s = 530.4 eV,[59] which was attributed to the contributions of O_I, O_{II}, and O_{III} bindings to Ca_I and Ca_{II} in the hydroxyapatite structure.[65] In addition, that O 1s = 530.4 eV has also contributions from the CO_3^{2-} groups bonded to Ca sites at the film surface. Following with the 180 min film analyses, the Figure 4d shows the Ca 2p peak fitting. The energy of Ca $2p_{3/2}$ = 347.3 eV was established for all Ca−O bindings: over the Ca_I and Ca_{II} sites at the HA atomic structure, for the Ca−Ca and Ca−OH bindings at the hydroxyapatite Ca_{II} sites.[59,61,65] The energy of Ca $2p_{3/2}$ = 346.2 eV was recognized as the Ca bonded to the oxygens from the carbonates groups (CO_3^{2-}) at the film surface.[48,59,61] Finally, the P 2p was fitted with two binding energy for the P $2p_{3/2}$ peak (Figure 4e): (i) the P $2p_{3/2}$ = 133.1 eV was established to the phosphor bonded to the oxygens in the $(PO_4)^{3-}$ groups, in the hydroxyapatite structure;[59,61] (ii) and the P $2p_{3/2}$ = 132.2 eV (Figure 4e) was attributed to other weak phosphor bonds,[64] probably from organic species at the surface.

The Ca/P ratio that was estimated by XPS (Ca/P = 1.68 ± 0.08) was very close to the HA stoichiometric value (Ca/P = 1.67), indicating that the Ca/P ratio of the film increased with deposition time and with film thickness. The CaO phase that was identified by XPS in thin films deposited for 30 s was not present in the thick films, as will be shown in the next section. These results reinforce the proposal that the transformation of ACP into HA nanodomains requires additional energy, which was continuously delivered to the primary cluster units by particle bombardment. The work by Lu and group[66] showed the dependencies between different calcium phosphates (octacalcium phosphate (OCP), tricalcium phosphate (TCP), and HA) using the ratios of the areas of the second peak satellite O $(1s)_{II}$ with respect to the total area of the oxygen spectrum in XPS. In our case, the ratio was $(O(1s)_{II}/O(1s)_{total})$ = 0.067, similar to that in the work by Lu et al.[66] which was 0.066. This result further confirms the strong similarity between the stoichiometry of a film 930 nm thick that is made by RAMS and that of a standard powder HA sample.[66]

3.2.2. Film Structure. The identification of the mineral phases that formed at the beginning of film crystallization was only possible with grazing-incidence X-ray diffraction (GIXRD) using synchrotron radiation. The GIXRD patterns of the fourth series of calcium phosphate films (Table 1) with deposition times less than and equal to 30 min, as shown in Figure 5a,

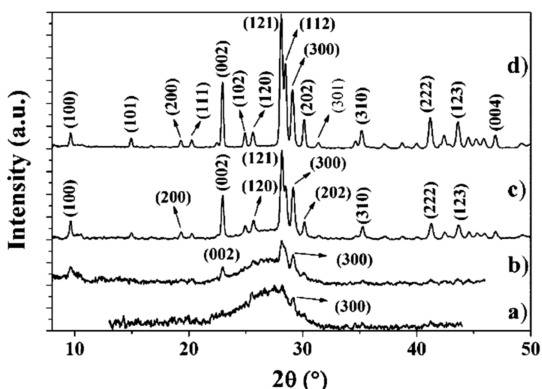

Figure 5. GIXRD (λ = 0.13775 nm) patterns at a grazing incidence of Φ = 0.5° for the films that were fabricated with thicknesses and deposition times of (a) 90 nm, 30 min; (b) 135 nm, 45 min; (c) 225 nm, 75 min; and (d) 540 nm, 180 min. The HA thin films were made at a deposition rate of 3 nm/min (Z = 13 mm) with a plasma power of 120 W and gas pressures of 5 mTorr and 1 mTorr for argon and oxygen.

exhibited a very broad region around 20° < 2θ < 30°, confirming that the film is possibly composed of an amorphous phase in the first minutes of deposition. The first sign of crystallization was observed in the films that were deposited for 30 min (90 nm thickness) by the presence of a weak peak at 2θ = 29.160°, which corresponds to the HA (300) plane. This narrow peak was superposed on the broad signal in 20° < 2θ < 30°, confirming the presence of crystalline HA nanodomains at the first stage of deposition.[67,68] As the deposition time increased, the broad region quickly decreased, while the main HA peaks appeared and increased in intensity, as shown in Figure 5b. After 75 min of deposition (225 nm thickness), as shown in Figure 5c, the film exhibited a GIXRD polycrystalline pattern. All of the indexed peaks coincided with the hexagonal ($P6_3/m$) HA phase (ICDD N° 84-1998).[43] Additionally, no other amorphous calcium phosphate phases or crystalline CaO were detected, reinforcing the hypothesis that HA nanodomains formed from ACP/CaO complexes.

The calculated ($a = b$ = 0.945 nm, c = 0.692 nm) unit cell parameters for the film that was deposited at 180 min, with a thickness of 540 nm (Figure 5d), were higher than those of HA crystallized in an aqueous media ($a = b$ = 0.942 nm, c = 0.688 nm), indicating the existence of strains[46,47,69] which are also commonly found in thin film structures. However, these defects did not disrupt the highly crystalline long-range order that was obtained from RAMS deposition. The ratio between the crystallite size that was obtained from GIXRD (73 nm) and the film thickness (540 nm), as shown in Figure 5d, was much higher than that of films produced from improved magnetron sputtering (MS) systems, in which this ratio was 0.03.[70] This experiment demonstrates that the energy and minimum time of deposition can be precisely tuned to grow nanocrystalline and crystalline HA films at 30 and 75 min (with a deposition rate of 3 nm/min (Table 1)) for a medium with an effective electron temperature and electron density of T_{eff} = 11.8 eV and n_e = 2.0 × 10^{15} m^{-3}.

To check the amorphous or nanocrystalline nature of the films at the first stage of deposition, a high resolution transmission electron microscopy (HRTEM) analysis was conducted using a 45 nm thick film (Table 1), which exhibited a typical amorphous GIXRD pattern. As described in section 2.4, HRTEM analysis was only possible because the sample was prepared with the focused ion beam (FIB) technique. The film thickness favored FIB preparation because it avoided an aggressive implantation of Pt ions throughout the entire thickness of the CaP film. The sample that was prepared by FIB, as shown in Figure 6a, was a multilayer that was composed

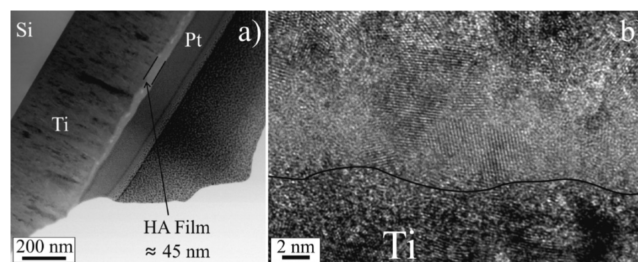

Figure 6. (a) Image obtained by scanning transmission electron microscopy (STEM; bright field imaging) for the sample that was prepared by FIB showing the CaP thin film region with a thickness of 45 nm between the Ti and Pt films. (b) HRTEM of the CaP thin film showing many HA crystalline nanodomains. The thin film was fabricated at 120 W of RF power, Z = 13 mm, a deposition rate of 3 nm/min, and gas pressures of 5 mTorr and 1 mTorr for argon and oxygen, respectively.

of (i) a Ti film produced by an e^- beam and deposited over Si, (ii) a 45 nm thick CaP coating, and (iii) a Pt film deposited by a Ga ion source. The HRTEM image in Figure 6b shows that the CaP layer was composed of crystalline nanodomains (≈2 nm) coexisting with highly disordered regions. The interplanar spacing (0.163, 0.173, 0.183, 0.213, 0.215, 0.222, 0.226, 0.229, 0.272, 0.277, and 0.281 nm) of these crystalline nanodomains was compatible with HA.[43] This evidence revealed that the broad peak that was observed in the 20° < 2θ < 30° region of the GIXRD pattern was due to a mixture of amorphous and very small crystalline nanodomains. The coexistence of the amorphous and crystalline phases reinforced the hypothesis

that the energy that was delivered by the plasma (T_{eff} = 11.8 eV) induced first the formation of ACP clusters and then their rapid transformation into HA crystalline nanodomains.

3.2.3. Dependence on Target Stoichiometry. The influence of the target stoichiometry on the composition of the films that were produced from the RAMS geometry was also investigated. For this investigation, a third series of films was deposited from multiphase targets that were constituted by HA, TCP and CaO. Surprisingly, a crystalline HA phase was always formed, as shown in the GIXRD patterns of Figure 7a. The existence of

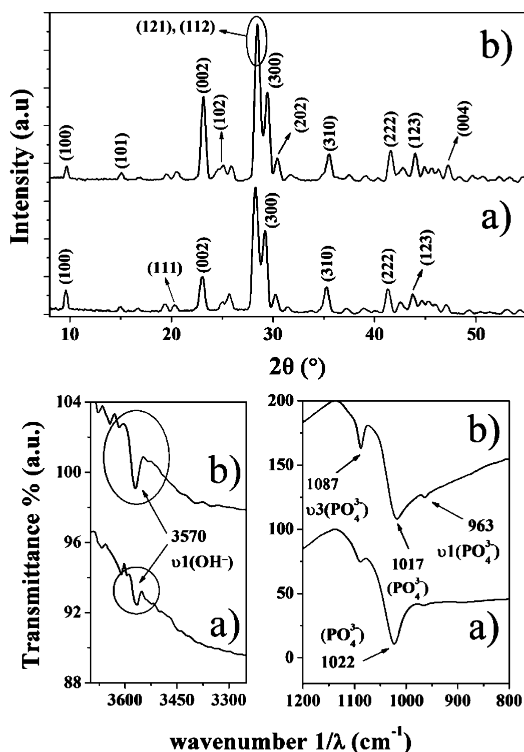

Figure 7. GIXRD (λ = 0.13775 nm) patterns at the grazing incidence of Φ = 0.5° (over) and FTIR spectra (under) of the films that were fabricated with a deposition time of 180 min: (a) thin film without thermal treatment and (b) thin film with thermal treatment at 800 °C for 2 h. The thin films were made at Z = 10 mm with a plasma power of 120 W and gas pressures of 5 mTorr and 1 mTorr for argon and oxygen.

amorphous phases, such as CaO or other calcium phosphate, was discarded because the GIXRD pattern of the same film after thermal treatment at 800 °C for 2 h in an argon atmosphere did not exhibit any additional crystalline phases besides HA, as shown in Figure 7b. The GIXRD and FTIR analyses confirmed the proposition in the preceding sections that the formation of HA is mainly dependent on the correct tuning of the plasma temperature in the region where the magnet field is $B \approx 0$ T (Z = 10 mm, T_{eff} = 11.7 eV).

3.2.4. Film Morphology. The film morphology during the early growth stage was evaluated using atomic force microscopy (AFM) measurements (fourth series of films, Table 1). For 5 min of deposition time, the film surface was covered by short particles with diameters varying from 40 to 370 nm (Figure 8a). The particle diameter distribution exhibited a Gaussian behavior with a maximum of approximately 115 ± 15 nm. The root-mean-square (RMS) roughness of 1.2 ± 0.4 nm was higher than the substrate roughness (0.25 ± 0.05 nm) and

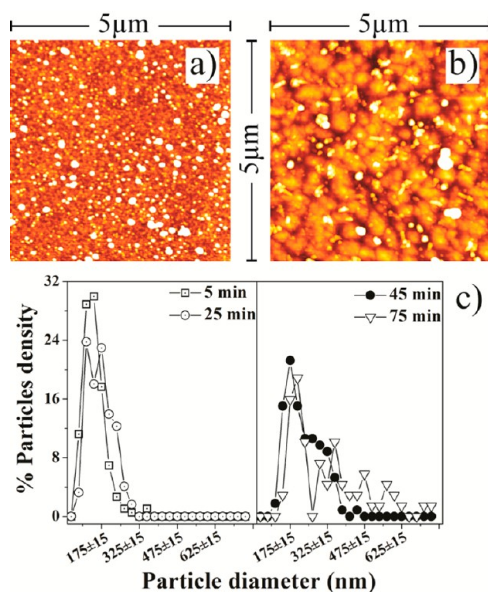

Figure 8. AFM images of the films taken in the tapping mode: (a) 5 min and (b) 75 min of deposition time. (c) Histograms of the particle diameters as determined from the AFM images for different deposition times (deposition rate of 3 nm/min). The plasma conditions were 120 W of power, Ar and O_2 gas pressures of 5 mTorr and 1 mTorr, respectively, and position Z = 13 mm (T_{eff} = 11.8 eV).

smaller than the film thickness (15 nm), suggesting that a thin layer of calcium phosphate clusters had already formed beneath the deposited particles at 5 min of deposition (Table 3). Figure 8b,c shows that the particle size distribution moved to higher diameters as the sputtering time increased. The growth of these HA crystalline domains was induced by the indirect increase of the temperature on the substrate surface, which was produced by the ions from the plasma sheath. Figure 8c also shows that the mode that was centered at low particle diameters remained for long deposition times, suggesting that small particles continued to form on the film surface during the whole deposition process. However, the particle growth did not affect the surface roughness, which remained constant, even for high film thicknesses, as shown in Table 3.

3.3. Plasma Glow Temperature Effect. The substrate position Z influenced the plasma glow properties (T_{eff}, n_e, and V_p) and consequently the deposition rate (particle flow on a wall). As shown in Table 2, T_{eff} varied slightly from 11.7 to 11.8 eV ($n_e \approx 2.0 \times 10^{15}$ m^{-3}) when Z increased from 10 to 13 mm. Therefore, the deposition rate changed from 5.2 to 3.0 nm/min when Z increased from 10 to 13 mm; this can be adjusted by monitoring the substrate position Z. Figure 9a,b shows that an increase in Z (decrease in the deposition rate) decreased the mean size of the HA grains and their surface crystallinity (as also shown in Figure 9a,b).

A fifth series of films was prepared to test the quality of the thin films that were produced by RAMS, which is highly dependent on the applied RF power level. This parameter also directly influences the plasma temperature and plasma density, which control the flux of the sputtered particles and the deposition rate. The GIXRD patterns of films that were produced with the RF power varying from 90 to 120 W showed peaks that were due to a single crystalline HA phase, as shown in Figure 10. The diffraction patterns also revealed a strong preferential orientation along the apatite (002) direction "*c*", especially for the 90 W RF power. The crystallite size increased

Table 3. Root Mean Square (RMS) Roughness of the Films That Were Produced at Different Deposition Times[a]

	samples					substrate
deposition time (min)	5	15	25	45	75	
thickness (nm)	15	45	75	135	225	
RMS roughness (3 μm × 3 μm), (nm)	1.2 ± 0.4	3.3 ± 0.9	1.2 ± 0.7	3.8 ± 1.9	4.4 ± 1.6	0.25 ± 0.05
RMS roughness (1 μm × 1 μm), (nm)	1.3 ± 0.6	1.8 ± 0.8	1.5 ± 1.4	1.7 ± 0.9	1.7 ± 0.9	0.25 ± 0.05

[a]The roughness was determined by AFM in the contact mode. The films were produced at 120 W of RF power, Ar and O2 pressures of 5 mTorr and 1 mTorr and position Z = 13 mm, respectively.

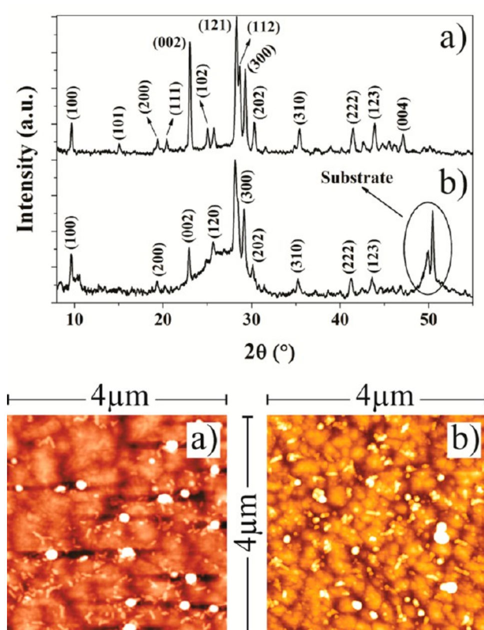

Figure 9. GIXRD (λ = 0.13775 nm) patterns at the grazing incidence of Φ = 0.5° (over) and AFM images of the film surfaces (under) at same deposition time of 60 min and at different effective temperatures of the plasma for (a) T_{eff} = 11.7 eV (deposition rate of 5.2 nm/min, film thickness of 312 nm, Z = 10 mm) and (b) T_{eff} = 11.8 eV (deposition rate of 3 nm/min, film thickness of 180 nm, Z = 13 mm). The plasma was made at 120 W of power and at Ar and O_2 gas pressures of 5 mTorr and 1 mTorr, respectively.

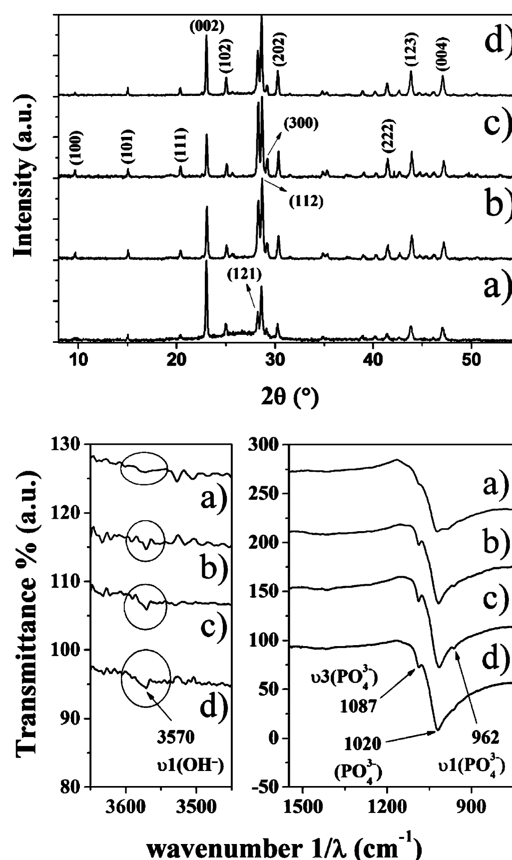

Figure 10. GIXRD (λ = 0.13775 nm) patterns at the grazing incidence of Φ = 0.5° (over) of the films that were made with different RF powers of (a) 90 W, (b) 100 W, (c) 110 W, and (d) 120 W. FTIR spectra in the region of hydroxyl and phosphate (under) of the films made at (a) 90 W, (b) 100 W, (c) 110 W, and (d) 120 W RF powers. The deposition time (180 min), gas pressures (argon at 5 mTorr and oxygen at 1 mTorr), and position Z = 10 mm were constant.

from 63 to 124 nm when the RF power increased from 90 to 120 W, indicating that the film crystallinity is directly dependent on the energy of the sputtered particle and on the physical properties (temperature, density and potential) of the plasma. The ratio between the crystallite size of the film (124 nm) and its thickness (930 nm), as shown in Figure 10d, was similar to that of the films that were made in the fourth series (films at 180 min of deposition time, Figure 5d). The dependence of the crystallinity on the RF power was confirmed by FTIR analyses. The positions of the PO_4^{3-} (964, 1019, and 1087 cm^{-1}) and OH^- (at 3570 cm^{-1}) bands became broader as the RF power decreased, suggesting an increase in the HA structure disorder.

This fifth series of films was also used to investigate the influence of the RF power on the morphology of the films. AFM images, which were taken in the tapping mode, showed that the crystalline films that were deposited for 180 min with the RF power varying from 90 to 120 W exhibited a grain structure with a maximum roughness of 8 nm (area of 100 μm^2), as shown in Figure 11a,b. The RMS roughness (R_q) increased from 4.7 to 8.4 nm (area of 100 μm^2) over the range of 90−120 W and saturated afterward. The most probable particle diameter, D_p, was 250 ± 50 nm for RF powers in the range of 90−100 W. For a higher power, the particle size distribution moved to larger D_p values, as shown in Figure 11c.

3. CONCLUSIONS

The magnetron sputtering system with two opposite magnetrons, RAMS, that was developed in this work generated a plasma, RF forwarded power of 120 W and argon and oxygen pressures of 5 mTorr and 1 mTorr, respectively, with adequate energy of $T_{eff} \approx 11.8$ eV and electron density of $n_e = 2.0 \times 10^{15}$ m^{-3} to produce a hydroxyapatite nanocoating at room temperature. Using this thermodynamic condition, it was possible to deposit crystalline HA films, at room temperature, on silicon substrates with thickness varying from 254 to 540 nm, crystallite mean size of 73 nm, and RMS roughness of 1.7 ± 0.9 nm. The physicochemical characteristics of the

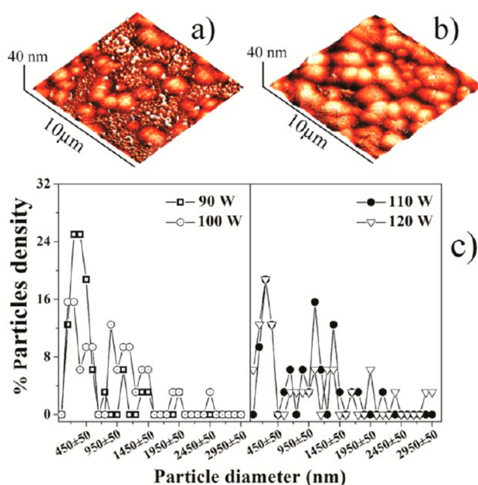

Figure 11. AFM topographic images of the HA films for an RF power of (a) 90 W and (b) 120 W. (c) Histograms of the particle diameters D_p for the samples with different powers supplied to the magnetrons.

hydroxyapatite coating revealed a higher sensitivity to the RAMS conditions than to the composition of the targets. By tuning the geometry and energy of the plasma besides the substrate-to-magnetron position (Z = 10 mm) relative to the magnetic field ($\boldsymbol{B}$ = 143 mT) and a substrate floating potential (2 V at Z position), it was possible to control and adjust the nanocoating stoichiometry and crystallinity. XPS measurements on films deposited for 30 s indicated that CaO and P_2O_5 species were deposited in the initial stage of the sputtering process. The deposition time was an essential parameter in delivering the necessary energy to transform these primary species into amorphous calcium phosphate *building units*, induce particle growth and the subsequent transformation into HA crystalline grain domains. These results suggested that the fabrication of high-quality nanostructured HA coating functionalized for biomedical applications by the magnetron sputtering technique is only possible if the main characteristics of the plasma are known and controlled.

AUTHOR INFORMATION

Corresponding Author

*E-mail: rossi@cbpf.br. Tel: +55-21-2141-7370.

Notes

The authors declare no competing financial interest.
The authors declare no competing financial interest.

ACKNOWLEDGMENTS

This project was supported by the Coordenação de Aperfeiçoamento de Pessoal de Nível Superior (CAPES) – Brazil and the Brazilian Center for Physics Research (CBPF); we thank the Brazilian Synchrotron Light Laboratory (LNLS) in Campinas – São Paulo for the use of XRD1 and XRD2 beamlines; Dr. Suzana Bottega Peripolli of the National Institute of Metrology (INMETRO) – Rio de Janeiro and Dr. João Paulo Sinnecker of the Brazilian Center for Physics Research (CBPF) for sample preparation using FIB and the use of COMSOL Multiphysic software (license 2072699), respectively, and Prof. Rolf Andreas Eichler for his kind support.

REFERENCES

(1) Morgan, H.; Wilson, R. M.; Elliott, J. C.; Dowker, S. E. P.; Anderson, P. *Biomaterials* **2000**, *21*, 617–627.
(2) Wang, L.; Nancollas, G. H. *Chem. Rev.* **2008**, *108*, 4628–4669.
(3) Paul, W.; Sharma, C. P. *Am. J. Biochem. Biotechnol.* **2006**, *2*, 41–48.
(4) Astala, R.; Stott, M. J. *Phys. Rev. B* **2008**, *78*, 075427.
(5) Iliescu, M.; Nelea, V.; Werckmann, J.; Mihailescu, I. N. *Surf. Coat. Technol.* **2004**, *187*, 131–140.
(6) Macaskie, L. E.; Yong, P.; Paterson-Beedle, M.; Thackray, A. C.; Marquis, P. M.; Sammons, R. L.; Nott, K. P.; Hall, L. D. *J. Biotechnol.* **2005**, *118*, 187–200.
(7) Wang, H.; Eliaz, N.; Xiang, Z.; Hsu, H. P.; Spector, M.; Hobbs, L. W. *Biomaterials* **2006**, *27*, 4192–4203.
(8) Ueda, K.; Narushima, T.; Goto, T.; Taira, M.; Katsube, T. *Biomed. Mater.* **2007**, *2*, S160–S166.
(9) Wen, C. E.; Xu, W.; Hu, W. Y.; Hodgson, P. D. *Acta Mater.* **2007**, *3*, 403–410.
(10) Dos Santos, E. A.; Moldovan, M. S.; Jacomine, L.; Mateescu, M.; Werckmann, J.; Anselme, K.; Mille, P.; Pelletier, H. *Mater. Sci. Eng., B* **2010**, *169*, 138–144.
(11) Ellies, L. G.; Nelson, D. G. A.; Featherstone, J. D. B. *Biomaterials* **1992**, *13*, 313–316.
(12) Khor, K. A.; Dong, Z. L.; Quek, C. H.; Cheang, P. *Mater. Sci. Eng., A* **2000**, *281*, 221–228.
(13) Dong, Z. L.; Khor, K. A.; Quek, C. H.; White, T. J.; Cheang, P. *Biomaterials* **2003**, *24*, 97–105.
(14) Guipont, V.; Jeandin, M.; Bansard, S.; Khor, K. A.; Nivard, M.; Berthe, L.; Cuq-Lelandais, J. P.; Boustie, M. *J. Biomed. Mater. Res., Part A* **2010**, *95A*, 1096–1104.
(15) Uchida, M.; Oyane, A.; Kim, H. M.; Kokubo, T.; Ito, A. *Adv. Mater.* **2004**, *16*, 1071–1074.
(16) Melde, B. J.; Stein, A. *Chem. Mater.* **2002**, *14*, 3326–3331.
(17) Zhang, K.; Francis, L. F.; Yan, H.; Stein, A. *J. Am. Ceram. Soc.* **2005**, *88*, 587–592.
(18) Padilla, S.; Román, J.; Carenas, A.; Vallet-Regí, M. *Biomaterials* **2005**, *26*, 475–483.
(19) Narayanan, R.; Seshadri, S. K.; Kwon, T. Y.; Kim, K. H. *Scr. Mater.* **2007**, *56*, 229–232.
(20) Wang, H.; Eliaz, N.; Hobbs, L. W. *Mater. Lett.* **2011**, *65*, 2455–2457.
(21) Liu, D.; Savino, K.; Yates, M. Z. *Surf. Coat. Technol.* **2011**, *205*, 3975–3986.
(22) Li, C.; Qi, L. *Angew. Chem., Int. Ed.* **2008**, *47*, 2388–2393.
(23) Li, C.; Hong, G.; Yu, H.; Qi, L. *Chem. Mater.* **2010**, *22*, 3206–3211.
(24) Joanni, E.; Ferro, M. C.; Mardare, C. C. *Mater. Res.* **2004**, *7*, 431–436.
(25) Carradò, A. *J. Coat. Technol. Res.* **2011**, *8*, 749–755.
(26) Rabiei, A.; Thomas, B.; Jin, C.; Narayan, R.; Cuomo, J.; Yang, Y.; Ong, J. L. *Surf. Coat. Technol.* **2006**, *200*, 6111–6116.
(27) Jeong, Y. H.; Choe, H. C.; Eun, S. W. *Thin Solid Films* **2011**, *519*, 7050–7056.
(28) Yang, Y.; Kim, K. H.; Ong, J. L. *Biomaterials* **2005**, *26*, 327–337.
(29) Boyd, A. R.; Meenan, B. J.; Leyland, N. S. *Surf. Coat. Technol.* **2006**, *200*, 6002–6013.
(30) Dorozhkin, S. V. *Prog. Biomater.* **2012**, *1*, 1–40.
(31) Surmenev, R. A. *Surf. Coat. Technol.* **2012**, *206*, 2035–2056.
(32) Nelea, V.; Morosanu, C.; Iliescu, M.; Mihailescu, I. N. *Surf. Coat. Technol.* **2003**, *173*, 315–322.
(33) Snyders, R.; Bousser, E.; Music, D.; Jensen, J.; Hocquet, S.; Schneider, J. M. *Plasma Processes Polym.* **2008**, *5*, 168–174.
(34) Van der Wal, E.; Wolke, J. G. C.; Jansen, J. A.; Vredenberg, A. M. *Appl. Surf. Sci.* **2005**, *246*, 183–192.
(35) Shi, J. Z.; Chen, C. Z.; Yu, H. J.; Zhang, S. J. *Bull. Mater. Sci.* **2008**, *31*, 877–884.
(36) Kim, W. G.; Choe, H. C. *Thin Solid Films* **2011**, *519*, 7045–7049.

(37) Hoshi, Y.; Naoe, M.; Yamanaka, S. *Jpn. J. Appl. Phys.* **1977**, *16*, 1715−1716.
(38) Hong, Z.; Luan, L.; Paik, S. B.; Deng, B.; Ellis, D. E.; Ketterson, J. B.; Mello, A.; Eon, J. G.; Terra, J.; Rossi, A. *Thin Solid Films* **2007**, *515*, 6773−6780.
(39) Mello, A.; Hong, Z.; Rossi, A. M.; Luan, L.; Farina, M.; Querido, W.; Eon, J.; Terra, J.; Balasundaram, G.; Webster, T.; Feinerman, A.; Ellis, D. E.; Ketterson, J. B.; Ferreira, C. L. *Biomed. Mater.* **2007**, *2*, 67−77.
(40) Holland, L.; Samuel, G. *Vacuum* **1980**, *30*, 267−274.
(41) Lieberman, M. A.; Lichtenberg, A. J. *Principles of Plasma Discharges and Materials Processing*, 2th ed.; John Wiley & Sons: Hoboken, NJ, 2005; pp 165−206.
(42) Popovic, R. S. *Sens. Actuators, A* **2000**, *85*, 9−17.
(43) Hughes, J. M.; Cameron, M.; Crowley, K. D. *Am. Mineral.* **1989**, *74*, 870−876.
(44) Cullity, B. D. *Elements of X-Ray Diffraction*; Cohen, M., Ed.; Addison−Wesley: Boston, MA, 1956; pp 309−310.
(45) Fullerton, E. E.; Schuller, I. K. *Phys. Rev. B* **1992**, *45*, 9292−9310.
(46) Yogamalar, R.; Srinivasan, R.; Vinu, A.; Ariga, K.; Bose, A. C. *Solid State Commun.* **2009**, *149*, 1919−1923.
(47) Venkateswarlu, K.; Bose, A. C.; Rameshbabu, N. *Phys. B* **2010**, *405*, 4256−4261.
(48) *Handbook of X-ray Photoelectron Spectroscopy*; Chastain, J., King, R. C., Eds.; Physical Electronics: Eden Prairie: MN, 1995.
(49) Stranak, V.; Herrendorf, A. P.; Drache, S.; Cada, M.; Hubicka, Z.; Bogdanowicz, R.; Tichy, M.; Hippler, R. *J. Appl. Phys.* **2012**, *112*, 093305.
(50) Ostrikov, K. *Rev. Mod. Phys.* **2005**, *77*, 489−511.
(51) Surmenev, R. A.; Surmeneva, M. A.; Evdokimov, K. E.; Pichugin, V. F.; Peitsch, T.; Epple, M. *Surf. Coat. Technol.* **2011**, *205*, 3600−3606.
(52) Ozeki, K.; Aoki, H.; Masuzawa, T. *J. Aust. Ceram. Soc.* **2010**, *46*, 59−62.
(53) Shaginyan, L. R.; Han, J. G.; Shaginyan, V. R.; Musil, J. *J. Vac. Sci. Technol., A* **2006**, *24*, 1083−1090.
(54) Sugden, T. M.; Schofield, K. *Trans. Faraday Soc.* **1966**, *62*, 566−575.
(55) Singh, R. B.; Rai, D. K. *J. Phys. Chem.* **1965**, *69*, 3461−3462.
(56) Treboux, G.; Layrolle, P.; Kanzaki, N.; Onuma, K.; Ito, A. *J. Phys. Chem. A* **2000**, *104*, 5111−5114.
(57) Milev, A.; Kannangara, G. S. K.; Ben-Nissan, B. *Mater. Lett.* **2003**, *57*, 1960−1965.
(58) Inoue, Y.; Yasumori, I. *Bull. Chem. Soc. Jpn.* **1981**, *54*, 1505−1510.
(59) Kaciulis, S.; Mattogno, G.; Pandolfi, L.; Cavalli, M.; Gnappi, G.; Montenero, A. *Appl. Surf. Sci.* **1999**, *151*, 1−5.
(60) Ying, W. B.; Mizokawa, Y.; Kamiura, Y.; Kawamoto, K.; Yang, W. Y. *Appl. Surf. Sci.* **2001**, *181*, 1−14.
(61) Landis, W. J.; Martin, J. R. *J. Vac. Sci. Technol., A* **1984**, *2*, 1108−1111.
(62) Demri, B.; Muster, D. *J. Mater. Process. Technol.* **1995**, *55*, 31−314.
(63) Combes, C.; Rey, C. *Acta Biomater.* **2010**, *6*, 3362−3378.
(64) Hoste, S.; Van de Vondel, D. F.; Van der Kelen, G. P. *J. Electron Spectrosc. Relat. Phenom.* **1979**, *17*, 191−195.
(65) Terra, J.; Jiang, M.; Ellis, D. E. *Philos. Mag. A* **2002**, *82*, 2357−2377.
(66) Lu, H. B.; Campbell, C. T.; Graham, D. J.; Ratner, B. D. *Anal. Chem.* **2000**, *72*, 2886−2894.
(67) Chow, L. C.; Sun, L.; Hockey, B. *J. Res. Natl. Inst. Stand. Technol.* **2004**, *109*, 543−551.
(68) Bigi, A.; Boanini, E.; Bracci, B.; Facchini, A.; Panzavolta, S.; Segatti, F.; Sturba, L. *Biomaterials* **2005**, *26*, 4085−4089.
(69) Zhang, J. M.; Zhang, Y.; Xu, K. W.; Ji, V. *Solid State Commun.* **2006**, *139*, 87−91.
(70) Xu, S.; Long, J.; Sim, L.; Diong, C. H.; Ostrikov, K. *Plasma Processes Polym.* **2005**, *2*, 373−390.